Available online at www.sciencedirect.com
SCIENCE DIRECT®
Journal of Sound and Vibration 289 (2006) 1045–1065
JOURNAL OF SOUND AND VIBRATION
www.elsevier.com/locate/jsvi

Receptance coupling for dynamics prediction of assemblies with coincident neutral axes

Tony L. Schmitz*, G. Scott Duncan

Department of Mechanical and Aerospace Engineering, University of Florida, P.O. Box 116300, Gainesville, FL 32611, USA

Received 26 January 2004; received in revised form 7 March 2005; accepted 10 March 2005
Available online 31 May 2005

Abstract

This paper details the prediction of flexural receptances for nested components with common neutral axes using a multiple-point receptance coupling approach. Numerical validation is included for different numbers of coupling coordinates, equal and unequal coordinate spacing, rigid and finite stiffness component connections, and component interface damping. Additionally, the sensitivity of the assembly response to noise in the component receptances is evaluated and it is shown that some data smoothing may be required if measured receptances are to be used to represent the individual components, rather than the analytic expressions provided here.

1. Introduction

Substructure analysis, or component mode synthesis, methods have been used for several decades to predict the dynamic response of complicated assemblies using measurements and/or models of the individual components, or substructures. These components can be represented by spatial mass, stiffness, and damping data, modal data, or receptances (i.e., frequency response functions) [1–13]. The latter representation may be preferred in situations where the assembly receptances are the desired analysis output. Prior receptance coupling studies have considered, for

*Corresponding author. Tel.: +1 352 392 8909; fax: +1 352 392 1071.
E-mail address: tschmitz@ufl.edu (T.L. Schmitz).

0022-460X/$ - see front matter © 2005 Elsevier Ltd. All rights reserved.
doi:10.1016/j.jsv.2005.03.006

example, plates with various supports [14–18], shells [19,20], plate-shell structures [21–23], mass loaded plates and shells [24], and machine tool structures [25–30].

In this work, the analytic receptance coupling method developed by Bishop and Johnson [1] is extended to the prediction of flexural (lateral vibration) receptances for assemblies composed of nested components with common neutral axes. The approach described here incorporates both translational and rotational degrees of freedom and can accommodate: (1) any number of connection coordinates with equal or unequal spacing; (2) non-uniform cross-sectional component geometries along the neutral axis, z, including asymmetry in the x and y directions; (3) non-rigid contact interfaces between components (including both stiffness and damping considerations); (4) variable stiffness and damping at different connection coordinates; (5) nonlinear interface stiffnesses [31,32]; and (6) viscous or hysteretic damping models.

2. Background and notation

Bishop and Johnson [1] presented closed-form receptance functions for the analysis of flexural vibrations of uniform Euler–Bernoulli beams with free, fixed, sliding, and pinned boundary conditions. For example, the direct receptances for the free–free beam shown in Fig. 1 due to externally applied harmonic forces $f_1(t)$ and $f_2(t)$, applied at coordinates $x_1(t)$ and $x_2(t)$, respectively, and moments $m_1(t)$ and $m_2(t)$, applied at $\theta_1(t)$ and $\theta_2(t)$, respectively, are

$$x_1 = h_{11}f_1, \quad x_1 = l_{11}m_1, \quad x_2 = h_{22}f_2, \quad x_2 = l_{22}m_2, \tag{1}$$

$$\theta_1 = n_{11}f_1, \quad \theta_1 = p_{11}m_1, \quad \theta_2 = n_{22}f_2, \quad \theta_2 = p_{22}m_2.$$

The corresponding cross receptances are

$$\begin{aligned} &x_1 = h_{12}f_2, \quad x_1 = l_{12}m_2, \quad x_2 = h_{21}f_1, \quad x_2 = l_{21}m_1, \\ &\theta_1 = n_{12}f_2, \quad \theta_1 = p_{12}m_2, \quad \theta_2 = n_{21}f_1, \quad \theta_2 = p_{21}m_1. \end{aligned} \tag{2}$$

Eqs. (1) and (2) can be written in matrix form and compactly represented using the notation shown as follows

$$\begin{Bmatrix} x_1 \\ \theta_1 \end{Bmatrix} = \begin{bmatrix} h_{11} & l_{11} \\ n_{11} & p_{11} \end{bmatrix} \begin{Bmatrix} f_1 \\ m_1 \end{Bmatrix} \quad \text{or} \quad \{u_1\} = [R_{11}]\{q_1\},$$

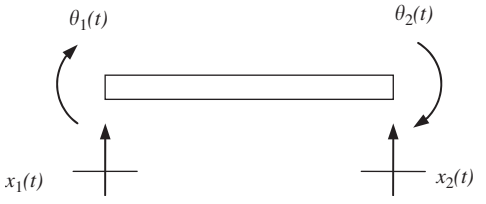

Fig. 1. Free–free beam coordinates.

$$\begin{Bmatrix} x_2 \\ \theta_2 \end{Bmatrix} = \begin{bmatrix} h_{221} & l_{22} \\ n_{22} & p_{22} \end{bmatrix} \begin{Bmatrix} f_2 \\ m_2 \end{Bmatrix} \quad \text{or} \quad \{u_2\} = [R_{22}]\{q_2\},$$
$$\begin{Bmatrix} x_1 \\ \theta_1 \end{Bmatrix} = \begin{bmatrix} h_{12} & l_{12} \\ n_{12} & p_{12} \end{bmatrix} \begin{Bmatrix} f_2 \\ m_2 \end{Bmatrix} \quad \text{or} \quad \{u_1\} = [R_{12}]\{q_2\},$$
$$\begin{Bmatrix} x_2 \\ \theta_2 \end{Bmatrix} = \begin{bmatrix} h_{21} & l_{21} \\ n_{21} & p_{21} \end{bmatrix} \begin{Bmatrix} f_1 \\ m_1 \end{Bmatrix} \quad \text{or} \quad \{u_2\} = [R_{21}]\{q_1\}, \tag{3}$$

where R_{ij} is the generalized receptance matrix that describes both translational and rotational component behavior [29]. The reader may note that R_{11} and R_{22} are symmetric and the R_{12} and R_{21} matrices are related by $R_{21} = \begin{bmatrix} h_{12} & n_{12} \\ l_{12} & p_{12} \end{bmatrix}$. The individual entries in these matrices depend on the boundary conditions and include contributions from both the rigid body (if applicable) and flexural modes. For example, at the left end of the free–free beam in Fig. 1, the R_{11} matrix terms are

$$h_{11}(\omega) = \frac{x_1}{f_1} = \frac{-(\cos\lambda L \sinh\lambda L - \sin\lambda L \cosh\lambda L)}{EI(1+\eta)\lambda^3(\cos\lambda L \cosh\lambda L - 1)},$$
$$l_{11}(\omega) = \frac{x_1}{f_1} = \frac{-(\sin\lambda L \sinh\lambda L)}{EI(1+\eta)\lambda^2(\cos\lambda L \cosh\lambda L - 1)},$$
$$n_{11}(\omega) = \frac{\theta_1}{f_1} = \frac{-(\sin\lambda L \sinh\lambda L)}{EI(1+\eta)\lambda^2(\cos\lambda L \cosh\lambda L - 1)},$$
$$p_{11}(\omega) = \frac{\theta_1}{m_1} = \frac{(\cos\lambda L \sinh\lambda L + \sin\lambda L \cosh\lambda L)}{EI(1+\eta)\lambda(\cos\lambda L \cosh\lambda L - 1)}, \tag{4}$$

where $\lambda = \left(\frac{m\omega^2}{LEI(1+i\eta)}\right)^{1/4}$, m is the beam mass (kg), ω is the frequency (rad/s), L is the beam length (m), E is the elastic modulus (N/m^2), I is the second area moment of inertia (m^4), and η is the structural damping factor[1] (unitless). These receptances can be used to couple components at their end points in order to determine assembly dynamics. For example, a free–free beam with diameter d_1 can be coupled to a second free–free beam with larger diameter d_2 to synthesize the receptances for a stepped shaft (see Fig. 2). The assembly flexural receptances, shown in Eq. (5) (the upper case variables denote assembly coordinates, forces, moments, and receptances), are determined by first writing the component displacements/rotations (see Eq. (6)).

$$\begin{Bmatrix} U_1 \\ U_2 \\ U_3 \end{Bmatrix} = \begin{bmatrix} G_{11} & G_{12} & G_{13} \\ G_{21} & G_{22} & G_{23} \\ G_{31} & G_{32} & G_{33} \end{bmatrix} \begin{Bmatrix} Q_1 \\ Q_2 \\ Q_3 \end{Bmatrix} \quad \text{where } U_1 = \begin{Bmatrix} X_i \\ \Theta_i \end{Bmatrix}, \tag{5}$$

$$G_{ij} = \begin{bmatrix} H_{ij} & L_{ij} \\ N_{ij} & P_{ij} \end{bmatrix} \quad \text{and} \quad Q_i = \begin{Bmatrix} F_i \\ M_i \end{Bmatrix},$$

[1]Damping was not included in Ref. [1], but has been added as part of this analysis.

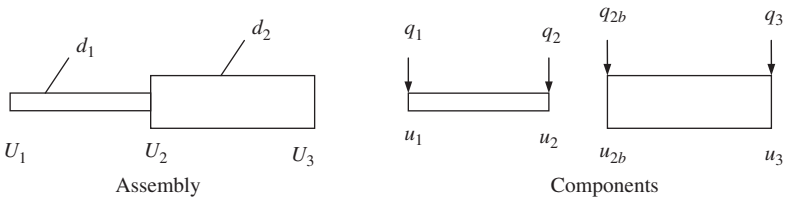

Fig. 2. Stepped shaft assembly and components. Diameters d_1 and d_2 are identified in the assembly schematic.

$$u_1 = R_{11}q_1 + R_{12}q_2, \quad u_2 = R_{21}q_1 + R_{22}q_2,$$

$$u_{2b} = R_{2b2b}q_{2b} + r_{2b3}q_3, \quad u_3 = R_{32b}q_{2b} + R_{33}q_3. \tag{6}$$

For the stepped shaft example, a rigid connection is applied at the interface and the compatibility conditions are written as

$$u_2 - u_{2b} = 0 \quad \text{and} \quad u_i = U_i, \qquad i = 1 \text{ to } 3, \tag{7}$$

where the latter expression specifies that the component and assembly coordinates are defined at the same spatial positions. The equilibrium conditions vary with the external force/moment location. To determine the first column of the assembly receptance matrix, Q_1 is applied to coordinate U_1. In this case, the equilibrium conditions are

$$q_2 + q_{2b} = 0, \; q_1 = Q_1 \quad \text{and} \quad q_3 = 0. \tag{8}$$

Substitution of the component displacements/rotations and equilibrium conditions into the compatibility conditions yields q_2 (see Eq. (9)). The expression for G_{11} is then given by Eq. (10). The other two first column receptances are determined in a similar manner. To find the receptances in the second and third columns, Q_2 must be applied to U_2 and Q_3 to U_3, respectively.

$$q_2 = -(R_{22} + R_{2b2b})^{-1}R_{21}Q_1, \tag{9}$$

$$G_{11} = \frac{U_1}{Q_1} = \frac{u_1}{Q_1} = \frac{R_{11}q_1 + R_{12}q_2}{Q_1} = R_{11} - R_{12}(R_{22} + R_{2b2b})^{-1}R_{21} = \begin{bmatrix} H_{11} & L_{11} \\ N_{11} & P_{11} \end{bmatrix}. \tag{10}$$

3. Concentric assembly coupling

In this paper, the end-to-end coupling described in the previous example is extended to multiple point coupling for concentric assemblies. The analysis is limited to nested assemblies with common neutral axes because only planar displacements in the lateral, or x and y, directions are considered and the relative displacements between components along the z direction are not modeled. If the component neutral axes are offset, the contact interface can experience sliding during flexural vibrations (similar to the pages of a paperback book when rolled into a tubular shape). This effect has been previously applied to increase damping during structural vibrations, but is not modeled here [33,34].

To demonstrate the coupling method, consider a rigid connection between a free–free internal cylinder and free–free external tube, where the internal cylinder's outer diameter is equal to the inner diameter of the external tube. Here, it is not sufficient to couple the two components only at their endpoints. The relative motions at coordinates along the assembly z-axis must also be constrained. The case of $n = 3$ connection coordinates, located at the assembly ends and at mid-length, will now be demonstrated. This gives a total of six component coordinates—three each on the internal cylinder and external tube (see Fig. 3).

The component displacement/rotations can be written as

$$\begin{aligned} u_1 &= R_{11}q_1 + R_{12}q_2 + R_{13}q_3, \quad u_2 = R_{21}q_1 + R_{22}q_2 + R_{23}q_3, \\ u_3 &= R_{31}q_1 + R_{32}q_2 + R_{33}q_3, \quad u_4 = R_{44}q_4 + R_{45}q_5 + R_{46}q_6, \\ u_5 &= R_{54}q_4 + R_{55}q_5 + R_{56}q_6, \quad u_6 = R_{64}q_4 + R_{65}q_5 + R_{66}q_6. \end{aligned} \tag{11}$$

The compatibility conditions for the rigid connection are

$$u_1 - u_4 = 0,\ u_2 - u_5 = 0 \quad \text{and} \quad u_3 - u_6 = 0 \tag{12}$$

and the component and assembly coordinates are defined at the same spatial locations so that $u_i = U_i$, $i = 1$ to 6. If the assembly direct response at the left end, $G_{11}(\omega)$, is to be determined, Q_1 is applied to coordinate U_1 of the assembly. The equilibrium conditions are then

$$q_1 + q_4 = Q_1,\ q_2 + q_5 = 0 \quad \text{and} \quad q_3 + q_6 = 0. \tag{13}$$

G_{11} is determined here using a matrix representation of the relevant equations. The first step is to insert the component displacement/rotation expressions into the compatibility conditions (see Eq. (14)).

$$\begin{aligned} R_{11}q_1 + R_{12}q_2 + R_{13}q_3 &= R_{44}q_4 + R_{45}q_5 + R_{46}q_6, \\ R_{21}q_1 + R_{22}q_2 + R_{23}q_3 &= R_{54}q_4 + R_{55}q_5 + R_{56}q_6, \\ R_{31}q_1 + R_{32}q_2 + R_{33}q_3 &= R_{64}q_4 + R_{65}q_5 + R_{66}q_6. \end{aligned} \tag{14}$$

The next step is to substitute $q_4 = Q_1 - q_1$, $q_5 = -q_2$, and $q_6 = -q_3$ and rearrange to obtain

$$\begin{bmatrix} R_{11} + R_{44} & R_{12} + R_{45} & R_{13} + R_{46} \\ R_{21} + R_{54} & R_{22} + R_{55} & R_{23} + R_{54} \\ R_{31} + R_{64} & R_{33} + R_{65} & R_{33} + R_{66} \end{bmatrix} \begin{Bmatrix} q_1 \\ q_2 \\ q_3 \end{Bmatrix} = \begin{bmatrix} R_{44} \\ R_{54} \\ R_{64} \end{bmatrix} \begin{Bmatrix} Q_1 \\ Q_1 \\ Q_1 \end{Bmatrix}, \tag{15}$$

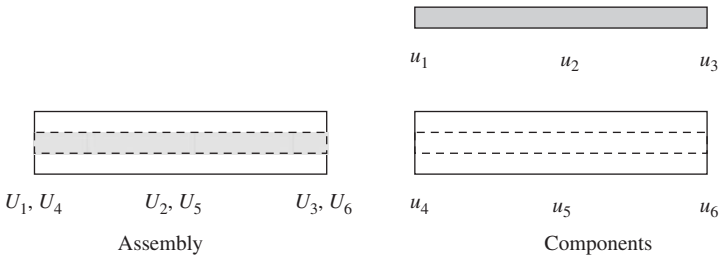

Fig. 3. Cylinder-in-tube assembly and components.

which gives the relationship between the component forces/moments and externally applied force/moment in matrix form. For this example, G_{11} can be expressed as

$$G_{11} = \frac{U_1}{Q_1} = \frac{u_1}{Q_1} = R_{11}\frac{q_1}{Q_1} + R_{12}\frac{q_2}{Q_1} + R_{13}\frac{q_3}{Q_1}, \tag{16}$$

so the ratios q_1/Q_1, q_2/Q_1, and q_3/Q_1 are required. These can be determined by rearranging Eq. (15) shown as follows

$$\begin{Bmatrix} q_1 \\ q_2 \\ q_3 \end{Bmatrix} \begin{Bmatrix} Q_1 \\ Q_1 \\ Q_1 \end{Bmatrix}^{-1} = \begin{bmatrix} R_{11}+R_{44} & R_{12}+R_{45} & R_{13}+R_{46} \\ R_{21}+R_{54} & R_{22}+R_{55} & R_{23}+R_{54} \\ R_{31}+R_{64} & R_{33}+R_{65} & R_{33}+R_{66} \end{bmatrix}^{-1} \begin{bmatrix} R_{44} \\ R_{54} \\ R_{64} \end{bmatrix} = [A], \tag{17}$$

where $[A]$ is a 6×2, or $2n \times 2 \times N$ matrix (N is the number of points in the frequency vector, ω). The reader may note that the matrix size is 6×2 because R_{ij} is a 2×2 matrix. The matrix A is partitioned as follows: the first two rows of A give q_1/Q_1; the second two rows provide q_2/Q_1; and the final two rows give q_3/Q_1. The desired direct receptances can then be computed from Eq. (16).

This three-point coupling example can be extended to n coupling points by recognizing the recursive pattern in Eq. (17). If the same coordinate numbering scheme is observed (see Fig. 4), the A matrix is given by Eq. (18).

$$[A] = \begin{bmatrix} R_{11}+R_{n+1,n+1} & R_{12}+R_{n+1,n+2} & \cdots & R_{1n}+R_{n+1,2n} \\ R_{21}+R_{n+2,n+1} & R_{22}+R_{n+2,n+2} & \cdots & R_{2n}+R_{n+2,2n} \\ \vdots & \vdots & \ddots & \vdots \\ R_{n1}+R_{2n,n+1} & R_{n2}+R_{2n,n+2} & \cdots & R_{nn}+R_{2n,2n} \end{bmatrix}^{-1} \begin{bmatrix} R_{n+1,n+1} \\ R_{n+2,n+1} \\ \vdots \\ R_{2n,n+1} \end{bmatrix}. \tag{18}$$

This matrix can again be partitioned to find q_1/Q_1, $q_2/Q_1, \ldots, q_n/Q_1$. The assembly receptances G_{11} can then be found using $G_{11} = R_{11}q_1/Q_1 + R_{12}q_2/Q_1 + \cdots + R_{1n}q_n/Q_1$. The following sections detail the development of the required receptances, R_{ij}, for the inner cylinder and outer tube.

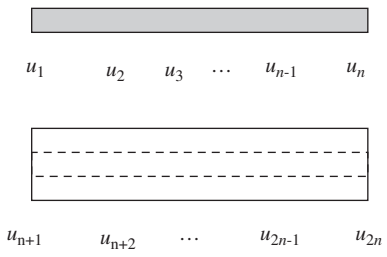

Fig. 4. Cylinder-in-tube component coordinates for n-point coupling.

3.1. Inner cylinder receptances

The inner cylinder receptance matrix is composed of n^2 R_{ij} terms ($i = 1$ to n and $j = 1$ to n). However, by observing the reciprocity relationships given in Section 2, it is only necessary to determine the upper triangular portion of the square R_{ij} matrix, or $\sum_{i=1}^{n} i$ terms.

The corners of the upper triangular portion of the matrix, R_{11}, R_{1n}, and R_{nn}, are found using the Bishop and Johnson [1] receptances directly, where the full beam length is used in these computations. The remaining terms in the first row of the R_{ij} matrix, $R_{12}, R_{13}, \ldots, R_{1,n-1}$ are determined next. To find R_{12}, q_2 is applied at coordinate u_2 as shown in Fig. 5.

The cylinder component must now be sectioned at coordinate u_2 into two elements with generalized receptance matrices E_{ij} and coordinates v_1 to v_n (see Fig. 5). For equally spaced connection coordinates, the length of the left element is $\Delta L = L/(n-1)$, while the right element length is $L - \Delta L$. The element displacements/rotations can be written as

$$v_1 = E_{12}s_2,\ v_2 = E_{22}s_2 \quad \text{and} \quad v_{2b} = E_{2b2b}s_{2b}, \tag{19}$$

where s_1, s_2, and s_{2b} are the non-zero element forces. The compatibility conditions for the rigid coupling between elements are given in Eq. (20). The associated equilibrium condition is provided in Eq. (21).

$$v_2 - v_{2b} = 0 \quad \text{and} \quad v_i = V_i, \qquad i = 1 \text{ to } n, \tag{20}$$

$$s_2 + s_{2b} = q_2. \tag{21}$$

Similar to the previous results, substitution of the element displacement/rotations and equilibrium condition into the compatibility conditions yields the following expression for R_{12}:

$$R_{12} = E_{12}(E_{22} + E_{2b2b})^{-1}E_{2b2b}. \tag{22}$$

To find R_{13}, q_3 is applied at u_3. The required left and right elements now have the lengths $2\Delta L$ and $L - 2\Delta L$, respectively. The equation for R_{13} is

$$R_{13} = E_{13}(E_{33} + E_{3b3b})^{-1}E_{3b3b}. \tag{23}$$

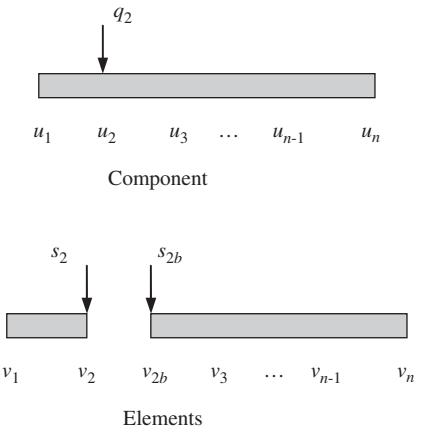

Fig. 5. Inner cylinder R_{12} determination.

The recursive pattern is immediately apparent so that R_{1j} is defined by

$$R_{1j} = E_{1j}(E_{jj} + E_{jbjb})^{-1}E_{jbjb}, \text{ where } j = 2 \text{ to } n-1 \text{ is the column number.} \tag{24}$$

Also, E_{1j} describes the cross receptances for the left element (with a length of $(j-1)\Delta L$), E_{ij} provides the direct receptances at the right end of the left element, and E_{jbjb} gives the direct receptances at the left end of the right element (with a length of $L-(j-1)\Delta L$).

The nth column of the R_{ij} matrix is defined next. In this case, q_n is applied to the coordinate u_n at the right end of the cylinder component in order to find R_{in}, where $i = 2$ to $n-1$ is the row number. The recursive form is

$$R_{in} = E_{ii}(E_{ii} + E_{ibib})^{-1}E_{ibn}, \tag{25}$$

where E_{ii} and E_{ibib} are defined in the same way as E_{jj} and E_{jbjb}, respectively. The E_{ibn} cross receptances for the right element are calculated using an element length of $L-(i-1)\Delta L$.

The next terms to describe are the on-diagonal receptances R_{ii}, $i = 2$ to $n-1$. These can be written as

$$R_{ii} = E_{ii}(E_{ii} + E_{ibib})^{-1}E_{ibib}. \tag{26}$$

Again, E_{ii}, the direct receptances at the right end of the left element and E_{ibib}, the direct receptances at the left end of the right element, have the same definitions as previously provided.

The remaining receptances are those R_{ij} terms above the on-diagonal, exclusive of the first row and nth column. These receptances are determined column-by-column. For a particular column, $j = 2$ to $n-1$, R_{ij} is given by

$$R_{ij} = E_{ij}(E_{jj} + E_{jbjb})^{-1}E_{jbjb}, \quad i = 2 \text{ to } j-1. \tag{27}$$

In this equation, the left element (with direct receptances E_{jj}) has a length of $(j-1)\Delta L$ and the right element (with direct receptances E_{jbjb}) has a length of $L-(j-1)\Delta L$. However, the E_{ij} element receptances cannot be determined directly from the Bishop and Johnson formulation [1]. In this case, subelement receptances S_{ij} must be defined. This is demonstrated by solving for R_{23}.

To find R_{23}, q_3 is applied to coordinate u_2. The cylinder component is then split at coordinate u_3 to define two elements (see Fig. 6). The element displacements/rotations are given by

$$v_2 = E_{23}s_3, \quad v_3 = E_{33}s_3, \quad \text{and} \quad v_{3b} = E_{3b3b}s_{3b}. \tag{28}$$

The rigid connection compatibility conditions are shown in Eq. (29) and the equilibrium condition in Eq. (30).

$$v_3 - v_{3b} = 0 \quad \text{and} \quad v_i = u_i, \qquad i = 1 \text{ to } n. \tag{29}$$

$$s_3 + s_{3b} = q_3. \tag{30}$$

Using these equations, it is found that

$$R_{23} = E_{23}(E_{33} + E_{3b3b})^{-1}E_{3bi3}. \tag{31}$$

As noted, E_{23}, the cross receptances at coordinate v_2 of the left element due to the application of s_3 at coordinate v_3, is determined by separating the left element (with a length of $(j-1)\Delta L$), into two subelements at coordinate v_2 (see Fig. 6). The length of the left subelement is $(i-1)\Delta L = (2-1)\Delta L = \Delta L$, while the length of the right subelement is $(j-i)\Delta L = (3-2)\Delta L = \Delta L$.

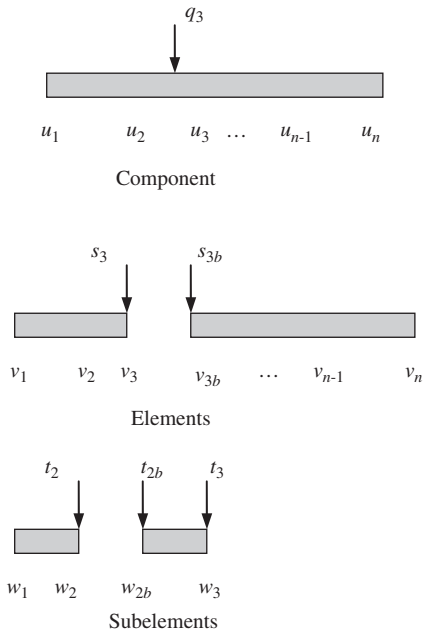

Fig. 6. Inner cylinder R_{23} determination.

Using the displacement/rotation, compatibility, and equilibrium equations, it is found that

$$E_{23} = S_{22}(S_{22} + S_{2b2b})^{-1} S_{2b3}, \tag{32}$$

where S_{22} gives the direct receptances at the right end of the left subelement, S_{2b2b} contains the direct receptances at the left end of the right subelement, and S_{2b3} represents the cross receptances for the right subelement. The recursive formulation for this equation is

$$E_{ij} = S_{ii}(S_{ii} + S_{ibib})^{-1} S_{ibj}, \ i = 2 \text{ to } j-1 \quad \text{and} \quad j = 2 \text{ to } n-1. \tag{33}$$

All terms in the upper triangular portion of the R_{ij} matrix for the inner cylinder have now been determined. The lower triangular portion, excluding the on-diagonal terms, is found by observing the symmetry rules given in Section 2 as demonstrated by the following pseudo-code.

for $i = 1$ to $n-1$
  for $j = i+1$ to n
    $R_{ij} = \begin{bmatrix} h_{ij} & l_{ij} \\ n_{ij} & p_{ij} \end{bmatrix}$
  next j
next i

3.2. Outer tube receptances

To find the R_{ij} matrix for the outer tube, n is added to each coordinate number (i.e., the coordinate number for left end of the tube is $n+1$ and the right end coordinate number is $2n$) and

the beam geometry and material properties are updated for the receptance computations. All other definitions remain the same.

3.3. Numerical results

To verify the method, cylinder and tube geometries with dissimilar material properties were chosen (see Table 1, where d_i and d_o are the inner and outer diameters, respectively, ρ is the density, and v is Poisson's ratio) and the assembly dynamics computed. A rigid coupling was selected in this case so that (analytical) verification calculations could be made using a composite beam approach.

To compute the composite beam frequency response, the equivalent modulus-area moment of inertia product, EI_{eq}, and mass, m_{eq}, values for the cylinder–tube assembly were calculated using Eqs. (34) and (35), where the t and c subscripts refer to the tube and cylinder, respectively. Eq. (4) was then used to calculate the free–free response at the left end of the assembly.

$$EI_{\text{eq}} = \frac{\pi}{64}(E_t(d_{0,t}^4 - d_{i,t}^4) + E_c d_{o,c}^4), \tag{34}$$

$$m_{\text{eq}} = \frac{\pi}{4}\left(\rho_t\left(d_{o,t}^2 - d_{i,t}^2\right) + \rho_c d_{o,c}^2\right)L. \tag{35}$$

A comparison between the analytical composite beam and $n = 3$ coupling results, as well as the more accurate Timoshenko beam solution, is shown in Fig. 7 (for brevity, only the displacement-to-force, or H_{11}, assembly results are shown, although all four direct receptances are predicted). It is seen that the 1000 Hz simulation frequency range (0.1 Hz resolution) captures the first three bending modes at 173.3, 476.9, and 932.7 Hz. For the long slender beam used in this numerical study, the Euler–Bernoulli composite beam results agree reasonably well with the Timoshenko beam solution (100 elements were used to represent the tube and cylinder as described in Appendix A) with increasing divergence visible in the second and third modes (0.25% and 0.49% errors, respectively). However, the three-point coupling result accurately predicts only the first bending mode. This can be explained by considering the mode shapes, $\Phi_k(x/L)$, for the first three bending modes, $k = 1, 2$, and 3, of a uniform free–free beam as shown in Fig. 8 [35]. It is seen that the central connection coordinate lies on a node for the second mode and insufficient points are

Table 1
Cylinder and tube parameters

	Inner cylinder	Outer tube
L (m)	0.500	0.500
d_i (m)	—	0.005
d_o (m)	0.005	0.010
ρ (kg/m^3)	14380	7800
E (N/m^2)	5.85×10^{11}	2.00×10^{11}
η	0.005	0.005
v	0.22	0.29

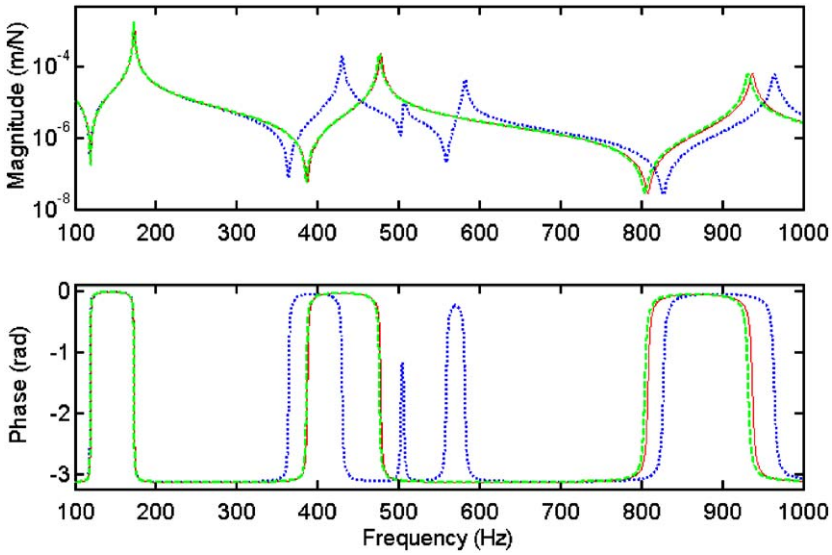

Fig. 7. Three-point coupling results (equal spacing). Results are shown for the three-point coupling of Euler–Bernoulli tube and cylinder (dotted line), Euler–Bernoulli composite cylindrical beam (solid), and Timoshenko composite beam (dashed).

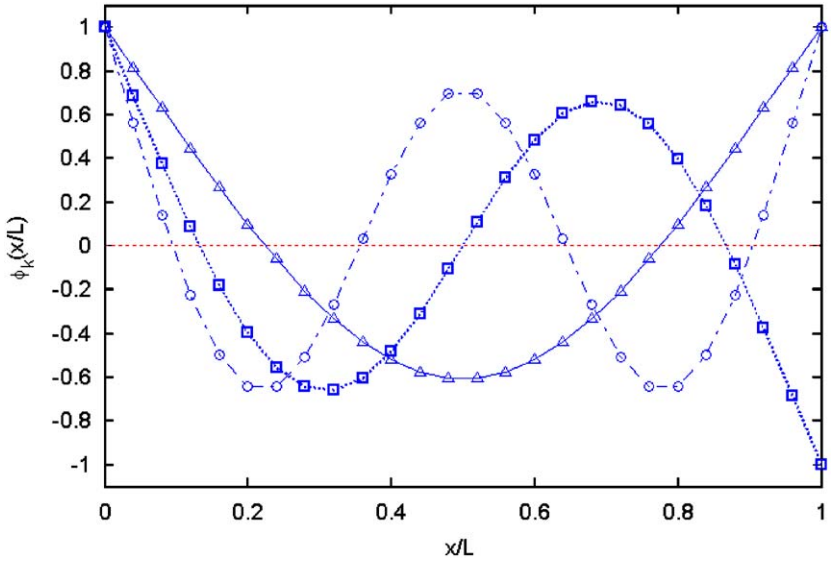

Fig. 8. First three bending modes for uniform free–free beam: $k = 1$ (triangles with solid line), $k = 2$ (squares with dotted line), and $k = 3$ (circles with dot-dashed line).

available to capture the third mode response. Using Shannon's sampling theorem (i.e., the Nyquist criterion) and these mode shapes, a general statement can be made about the number of required coupling coordinates. Considering the second mode shape, for example, this odd

function (about the beam midpoint) is similar in shape to a single period of a sine wave. To avoid aliasing, two spatial sampling points are required. However, connection coordinates at the assembly end points are also used by default, so the total required number of coordinates can be taken to be $n = k + 2$, where k is the mode number. This requirement is demonstrated in Fig. 9, where the coupling results for $n = 4$ and $n = 5$ are superimposed on the composite beam solution. It is seen that the $n = 2 + 2 = 4$ result captures the second mode behavior, but not the third mode. Similarly, the $n = 3 + 2 = 5$ result predicts all three modes with reasonable accuracy. Improved accuracy is obtained as n increases; coupling results and residual error (relative to the composite beam approach) for $n = 7$ are shown in Fig. 10. The larger error seen in the third mode is not due to a misrepresentation of the magnitude and phase curve shapes, but rather a shift in the predicted resonant frequency of 1.9 Hz to the left.

3.4. Unequal coordinate spacing

The coupling approach described here does not require equal spacing of the connection coordinates. Any convenient spacing can be selected; the only necessary modification to the procedure is that the derivation of the component receptances (described in Sections 3.1 and 3.2) must now take into account the coordinate locations to calculate the element and subelement lengths. Different criteria could be applied to select preferred coupling coordinate locations for the cylinder-in-tube example. Here, connection coordinates have been placed at the local, or relative, maxima and minima of the free–free beam mode shapes shown in Fig. 8, as well as at the component ends (which leads to unequal coordinate spacing). The local maxima/minima were identified by finding the zero crossings for the mode shape spatial derivatives, $d\Phi_k/dx$. The dimensionless x/L locations for these points are shown in Table 2.

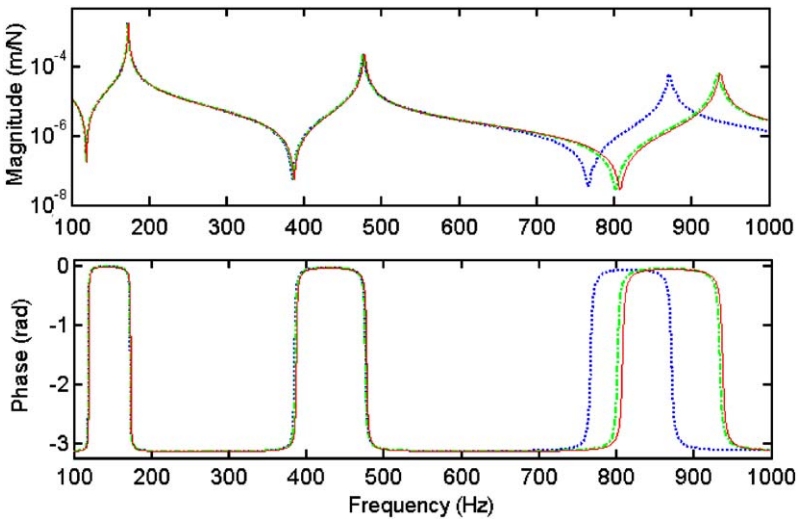

Fig. 9. Four- and five-point coupling results (equal spacing). Results are shown for Euler–Bernoulli composite beam (solid line), $n = 4$ (dotted), and $n = 5$ (dot-dashed).

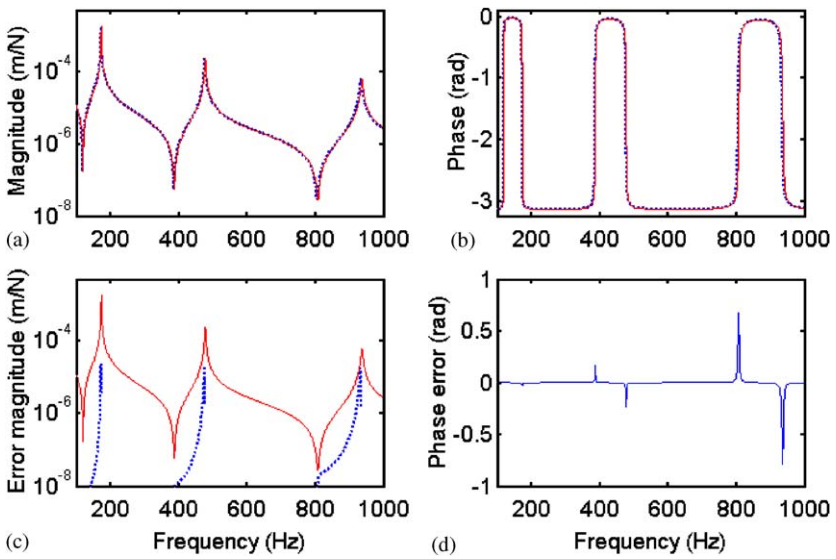

Fig. 10. Seven-point coupling result: (a) magnitudes for composite beam (solid line) and $n = 7$ (dotted); (b) corresponding phases; (c) residual error for $n = 7$ (dotted) with composite beam response (solid); (d) phase error.

Table 2
Locations for mode shape local maxima and minima

k	$\frac{x}{L}$ for $\frac{d\Phi_k}{dx} = 0$
1	0.5000
2	0.3084
	0.6916
3	0.2200
	0.5000
	0.7800

Comparisons between equal and unequal coordinate spacing are provided in Fig. 11. The dynamic response magnitudes and errors for $n = 4$ are shown in the left column, while the $n = 5$ results are given in the right column. For $n = 4$, the $k = 2$ connection coordinate locations were selected from Table 2. For $n = 5$, the $k = 3$ locations were applied. Close inspection of the errors between the unequal/equal coordinate spacing and composite beam receptances shows that the unequal coordinate spacing approach offers improved accuracy for the mode used to define the coordinate locations (i.e., the $n = 4$ results show smaller mode 2 error for the unequal spacing approach). However, the accuracy for lower-order modes tends to suffer (i.e., the $n = 4$ results show larger mode 1 error for the unequal spacing approach). In any case, since the mode shapes for more complicated assemblies are generally not known a priori, the equal coordinate spacing method may be the more practical choice.

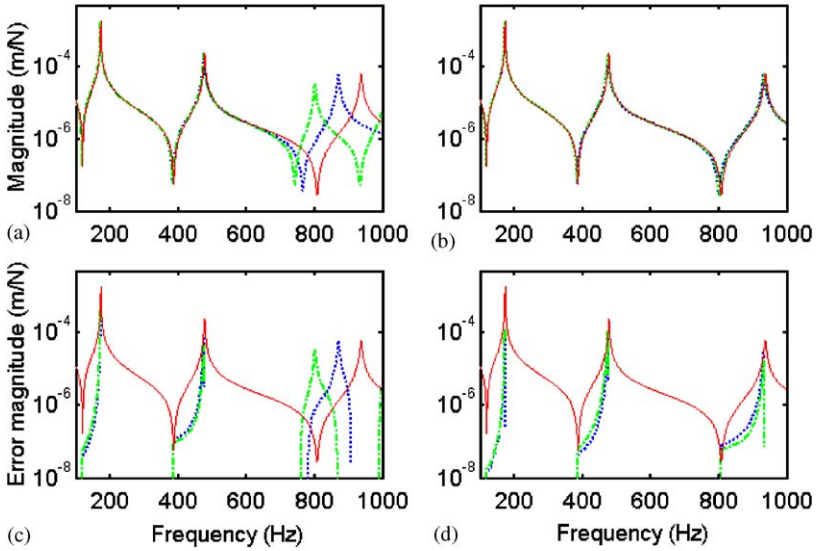

Fig. 11. Coupling results for equal and unequal connection coordinate spacing: (a) $n = 4$, magnitudes for composite beam (solid line), unequal (dotted), and equal spacing (dot-dashed); (b) $n = 5$ magnitudes; (c) $n = 4$ residual errors with composite beam response (solid); (d) $n = 5$ errors.

4. Non-rigid coupling

In the case of finite stiffness and non-zero damping[2] at the contact interface between the inner and outer components, the compatibility conditions must be modified to reflect the new coordinate displacement/rotation relationships. To demonstrate, the three-point free–free inner cylinder–outer tube coupling described in Section 3 will again be considered. Eq. (12) is now rewritten as

$$K(u_4 - u_1) = -q_4,\ K(u_5 - u_2) = -q_5 \quad \text{and} \quad K(u_6 - u_3) = -q_6, \tag{36}$$

where the complex stiffness matrix is defined as $K = \begin{bmatrix} K_x + i\omega c_x & 0 \\ 0 & k_\theta + i\omega c_\theta \end{bmatrix}$ for a viscous damping model [36]. In this matrix, the translational stiffness and damping terms, k_x and c_x, respectively, appear as constants; however, these terms may also be frequency-dependent and nonlinear [31,32]. The same is true for the rotational terms k_θ and c_θ. Additionally, although a single K matrix is identified in Eq. (36), each coupling location could use a different set of stiffness and damping values.

To find the direct receptances at the left end of the three-point coupled assembly, Q_1 is again applied to U_1 (the corresponding equilibrium conditions are provided in Eq. (13)). After inserting the component displacement/rotation expressions (Eq. (11)) and equilibrium conditions into

[2]The contact damping is generally thought to be the result of non-conservative asperity-level slip, or micro-slip, where some, but not all, of the asperity-level contacts exhibit relative motion during vibration.

Eq. (36) and rearranging, a modified version of Eq. (17) is obtained

$$\begin{Bmatrix} q_1 \\ q_2 \\ q_3 \end{Bmatrix} \begin{Bmatrix} Q_1 \\ Q_1 \\ Q_1 \end{Bmatrix}^{-1} = \begin{bmatrix} R_{11}+R_{44}+K^{-1} & R_{12}+R_{45} & R_{13}+R_{46} \\ R_{21}+R_{54} & R_{22}+R_{55}+K^{-1} & R_{23}+R_{54} \\ R_{31}+R_{64} & R_{32}+R_{65} & R_{33}+R_{66}+K^{-1} \end{bmatrix}^{-1} \begin{bmatrix} R_{44}+K^{-1} \\ R_{54} \\ R_{64} \end{bmatrix} = [A], \tag{37}$$

where the only difference is that the inverted K matrix is now summed with the component direct receptances. The solution procedure for the assembly receptances and derivation of the component receptances remain the same.

As an example, the component geometries and material properties given in Table 1 were again used, but the components were coupled through three non-rigid, damped connections. The stiffness and damping values were modified using two scenarios: (A) variable stiffness, zero damping; and (B) constant stiffness, variable damping. Additionally, it was verified that for very large stiffness values, the predicted assembly receptance approached the rigid result shown in Fig. 7 and for very small stiffness values, the predicted receptance approached the free–free cylinder result.

4.1. Case A: variable stiffness, zero damping

The first step in completing the assembly receptance predictions was to determine a working range for the translational and rotational stiffness values. It was decided to set the nominal translational spring constant equal to the first mode bending stiffness for the free–free inner cylinder and vary about this point. From Ref. [35], the first mode stiffness for lateral vibration of a uniform, free–free beam can be written as $k_x = (4.73004074)^4 EI/L^3$. For the inner cylinder properties given in Table 1, $k_x = 71871.3\,\mathrm{N/m} \cong 7 \times 10^4\,\mathrm{N/m}$. As an approximation, the rotational stiffness was taken to be equal to the product of k_x and the cylinder length, L. Fig. 12 shows the comparison between the rigidly coupled result and three different stiffness values: $k_x = \{7 \times 10^5,\ 7 \times 10^4,$ and $7 \times 10^3\}\,\mathrm{N/m}$. The expected trend of reduced resonant frequency with decreasing stiffness is observed.

4.2. Case B: constant stiffness, variable damping

For these predictions, constant k_x and k_θ values were applied ($7 \times 10^4\,\mathrm{N/m}$ translational stiffness case from Section 4.1). The c_x and c_θ values were selected using a dimensionless damping ratio, ζ, notation. The c_x value was determined from $c_x = 2\zeta\sqrt{k_x m}$, where m is the inner cylinder mass. Similarly, the c_θ value was calculated using $c_\theta = 2\zeta\sqrt{k_\theta J}$, where J is the inner cylinder mass moment of inertia, or $mL^2/12$ for the long, slender cylinder used in this numerical study. Fig. 13 shows the results for ζ values of 0, 0.01, 0.1, and 0.5. As expected, increasing damping ratios lead to decreased response amplitudes.

5. Noise effects

Because a primary use for receptance coupling methods is the direct joining of measured frequency response functions, the previous analyses were repeated in the presence of

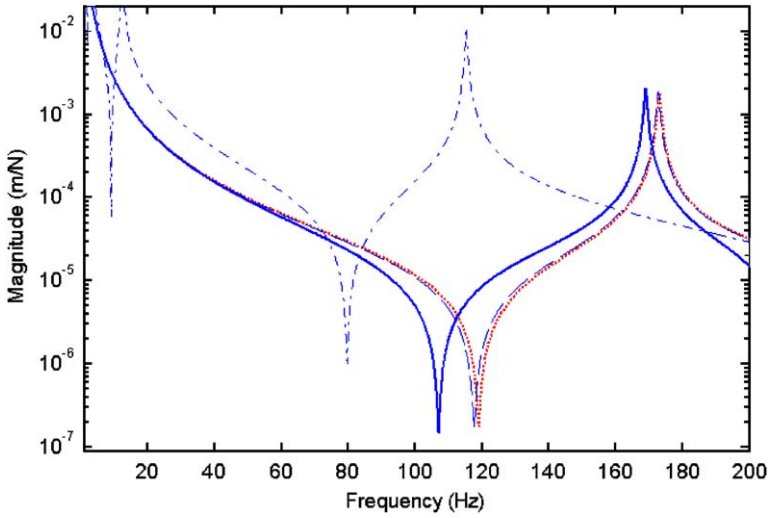

Fig. 12. Three-point, finite stiffness coupling example (zero damping). Results are provided for the following connection stiffness values: rigid (dotted line), 7×10^5 N/m (dashed), 7×10^4 N/m (solid), and 7×10^3 N/m (dot-dashed).

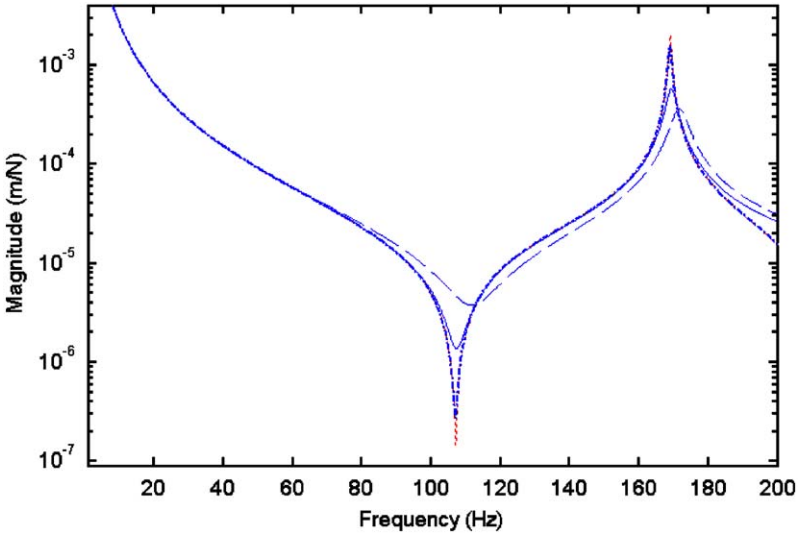

Fig. 13. Three-point coupling with non-zero damping (constant stiffness). Results are shown for damping ratios of: zero (dotted line), 0.01 (dot-dashed), 0.1 (solid), and 0.5 (dashed).

normally-distributed, 1% and 5% random noise. Fig. 14 compares the composite beam response (no noise) with results for rigid coupling—no damping and finite stiffness coupling—10% damping ($k_x = 7 \times 10^4$ N/m and $\zeta = 0.1$). The 1% noise level results are provided in the top panel (a) and 5% results in the middle panel (b). For the 1% case, little assembly noise is seen for both the rigid and finite stiffness/damped responses, although some noise is observed near the anti-resonance (more than an order of magnitude smaller than the resonance peak). In the 5%

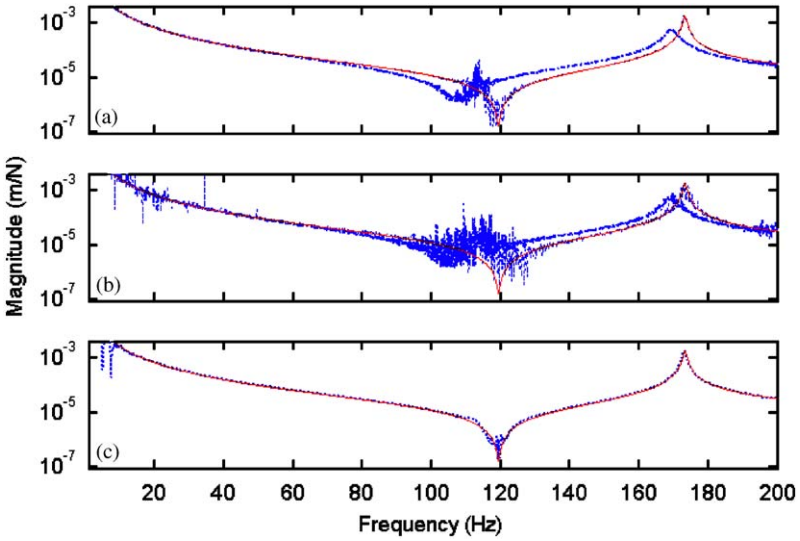

Fig. 14. Effect of noise on assembly response: (a) magnitudes for 1% noise added to component receptances—composite beam with no noise (solid line), rigid connection (dotted), and finite stiffness—10% damping (heavy dot-dashed); (b) 5% noise; (c) filtered 5% noise—rigid connection (dotted).

case, however, the predicted assembly response is virtually unusable with significant noise content across the full frequency range. This sensitivity to component receptance noise is most likely due to the required matrix inversion (see Eqs. (17), (18), and (37)). Practically, these results show that data smoothing may be required if measured frequency responses, rather than the analytic expressions applied here, are used as the component receptances. An example of data smoothing using a Savitzky–Golay (polynomial) filter, which performs a local polynomial regression to determine the smoothed value for each data point, is shown in the bottom panel (c). The component receptances with 5% random noise were first filtered using a polynomial order of 3 and frame size of 125 samples and then coupled using a rigid connection. It is seen that the assembly response noise has been strongly attenuated compared to the middle panel, rigid coupling result (b).

6. Non-uniform component cross-sections

So far only components with uniform cross-sections have been considered. The n-point coupling method can also be applied to join concentric components with continuously varying or stepped cross-sections. Consider the inner stepped shaft-outer cone assembly shown in Fig. 15. In this case, the inner stepped shaft can be synthesized as shown in Section 2. The cone is also separated into multiple sections (shown schematically by the vertical dotted lines in Fig. 15), similar to the finite element approach, and rigidly coupled. The sections lengths must be sufficiently small to effectively capture the changing cross-sectional geometry; however, the Bishop and Johnson closed-form expressions [1] include all mode shapes so it is not necessary to approximate the actual response using a finite number of modes. Once the individual component

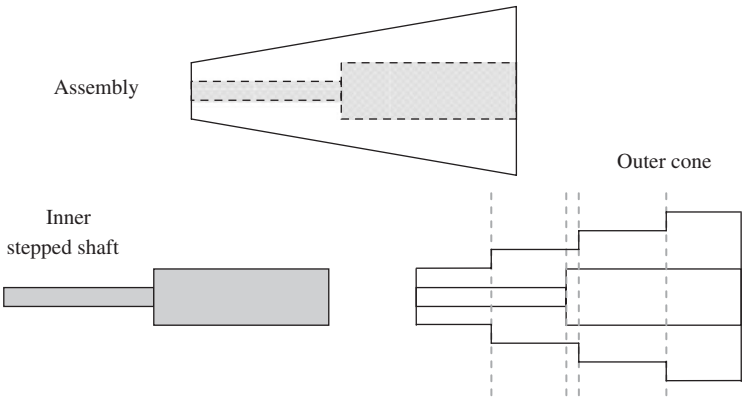

Fig. 15. Example of non-uniform cross-section components. The component receptances are first determined by rigidly coupling segments with different cross-sections. The assembly response is then found by joining the components using n-point coupling.

models are complete, they can then be joined using the n-point coupling approach described in the previous sections. As a final note, if the component cross-sections are not symmetric, different component models can be developed for the x and y directions, for example, and the coupling procedure completed separately for each direction.

7. Conclusions

This paper describes the use of receptance coupling techniques to predict flexural receptances for assemblies composed of nested components with common neutral axes. Through numerical studies, the approach was validated for different numbers of coupling coordinates, equal and unequal coordinate spacing, rigid and finite stiffness component connections, and component interface damping. Additionally, the sensitivity to noise in the component receptances was evaluated and it was found that some data smoothing may be required if measured receptances are to be used to represent the individual components.

Acknowledgements

The authors gratefully acknowledge partial financial support for this research from the National Science Foundation (DMI-0238019) and Office of Naval Research (2003 Young Investigator Program), as well as technical contributions from Dr. T. Burns, National Institute of Standards and Technology, Gaithersburg, MD.

Appendix A. Timoshenko beam solution

The Timoshenko beam model, which includes the effects of rotary inertia and shear, was implemented using finite elements [37]. Each four-degree-of-freedom (rotation and displacement

at both ends) free–free beam section was modeled using appropriate mass, M, and complex stiffness, K, matrices [38]. The mass matrix was

$$M = \frac{\rho A l}{(1+\phi)^2}\begin{bmatrix} \frac{13}{35}+\frac{7\phi}{10}+\frac{\phi^2}{3} & \left(\frac{11}{210}+\frac{11\phi}{120}+\frac{\phi^2}{24}\right)l & \frac{9}{70}+\frac{3\phi}{10}+\frac{\phi^2}{6} & -\left(\frac{13}{420}+\frac{3\phi}{40}+\frac{\phi^2}{24}\right)l \\ & \left(\frac{1}{105}+\frac{\phi}{60}+\frac{\phi^2}{120}\right)l^2 & \left(\frac{13}{420}+\frac{3\phi}{40}+\frac{\phi^2}{24}\right)l & -\left(\frac{1}{140}+\frac{\phi}{60}+\frac{\phi^2}{120}\right)l^2 \\ & & \frac{13}{35}+\frac{7\phi}{10}+\frac{\phi^2}{3} & -\left(\frac{11}{210}+\frac{11\phi}{120}+\frac{\phi^2}{24}\right)l \\ \text{Symmetric} & & & \left(\frac{1}{105}+\frac{\phi}{60}+\frac{\phi^2}{120}\right)l^2 \end{bmatrix}$$

$$+\frac{\rho A l}{(1+\phi)^2}\left(\frac{r_g}{l}\right)^2\begin{bmatrix} \frac{6}{5} & \left(\frac{1}{10}-\frac{\phi}{2}\right)l & -\frac{6}{5} & \left(\frac{1}{10}-\frac{\phi}{2}\right)l \\ & \left(\frac{2}{15}+\frac{\phi}{6}+\frac{\phi^2}{3}\right)l^2 & -\left(\frac{1}{10}-\frac{\phi}{2}\right)l & -\left(\frac{1}{30}+\frac{\phi}{6}+\frac{\phi^2}{6}\right)l^2 \\ & & \frac{6}{5} & -\left(\frac{1}{10}-\frac{\phi}{2}\right)l \\ \text{Symmetric} & & & \left(\frac{2}{15}+\frac{\phi}{6}+\frac{\phi^2}{3}\right)l^2 \end{bmatrix},$$

where A is the cross-sectional area, l is the section length, r_g is the radius of gyration, and ϕ is a shear deformation parameter given by $\phi = 12EI(1+\eta)/k'GAl^2$, where $G = E/2(1+\nu)$ is the shear modulus and k' is the shear coefficient which depends on the cross-section shape and ν [39]. The composite beam properties were incorporated as shown in Eqs. (34) and (35). The complex stiffness matrix (which included damping) was

$$K = \frac{EI(1+i\eta)}{l^3(1+\phi)^2}\begin{bmatrix} 12 & 6l & -12 & 6l \\ & (4+2\phi+\phi^2)l^2 & -6l & (2-2\phi-\phi^2)l^2 \\ & & 12 & -6l \\ \text{Symmetric} & & & (4+2\phi+\phi^2)l^2 \end{bmatrix}$$

$$+\frac{k'AG\phi^2}{4l(1+\phi)^2}\begin{bmatrix} 4 & 2l & -4 & 2l \\ & l^2 & -2l & l^2 \\ & & 4 & -2l \\ \text{Symmetric} & & & l^2 \end{bmatrix}.$$

The element M and K matrices were then collected into the global mass, $\boldsymbol{M}$, and complex stiffness, $\boldsymbol{K}$, matrices using Guyan reduction [37] and the resulting equation of motion solved in the frequency domain. See Eq. (A.1), where n elements have been applied.

$$[-\boldsymbol{M}\omega^2 + \boldsymbol{K}] \cdot \begin{bmatrix} x_1 \\ \theta_1 \\ x_2 \\ \theta_2 \\ \vdots \\ x_{n+1} \\ \theta_{n+1} \end{bmatrix} = \begin{bmatrix} f_1 \\ m_1 \\ f_2 \\ m_2 \\ \vdots \\ f_{n+1} \\ m_{n+1} \end{bmatrix}. \tag{A.1}$$

References

[1] R.E.D. Bishop, D.C. Johnson, *The Mechanics of Vibration*, Cambridge University Press, Cambridge, 1960.

[2] W.C. Hurty, Dynamic analysis of structural systems using component modes, *AIAA Journal* 3 (4) (1965) 678–685.

[3] A.L. Klosterman, J.R. Lemon, Building block approach to structural dynamics, *American Society of Mechanical Engineering Annual Vibration Conference*, publication VIBR-30, 1969.

[4] A.L. Klosterman, W. McClelland, I. Sherlock, *Dynamic Simulation of Complex Systems Utilizing Experimental and Analytical Techniques*, ASME Publication 75-WA/Aero-9, 1977.

[5] D.J. Ewins, Analysis of modified or coupled structures using FRF Properties, Internal Report 86002, Dynamics Section, Department of Mechanical Engineering, Imperial College, London, 1986.

[6] B. Jetmundsen, R.L. Bielawa, W.G. Flannelly, Generalized frequency domain substructure synthesis, *Journal of the American Helicopter Society* 33 (1988) 55–64.

[7] D. Otte, J. Leuridan, H. Grangier, R. Aquilina, Prediction of the dynamics of structural assemblies using measured FRF data: some improved data enhancement techniques, *Proceedings of the Nineth International Modal Analysis Conference* (IMAC-1991), Florence, Italy, 1991, pp. 909–918.

[8] C. Farhat, M. Geradin, A hybrid formulation of a component mode synthesis method, *33rd SDM Conference*, AIAA paper 92-2383-CP, Dallas, TX, 1992, pp. 1783–1796.

[9] Y. Ren, C.F. Beards, A generalized receptance coupling technique, *Proceedings of the 11th International Modal Analysis Conference* (IMAC-1993), Kissimmee, FL, 1993, pp. 868–871.

[10] Y. Ren, C.F. Beards, On substructure synthesis with FRF data, *Journal of Sound and Vibration* 185 (1995) 845–866.

[11] D.J. Ewins, *Modal Testing: Theory Practice and Application*, second ed., Research Studies Press, Philadelphia, PA, 2000.

[12] R.R. Craig Jr., A brief tutorial on substructure analysis and testing, *Proceedings of the 18th International Modal Analysis Conference* (IMAC-2000), San Antonio, TX, 2000, pp. 899–908.

[13] W. Lui, D.J. Ewins, Substructure synthesis via elastic media, *Journal of Sound and Vibration* 257 (2) (2002) 361–379.

[14] S. Azimi, Axisymmetric vibration of point-supported circular plates, *Journal of Sound and Vibration* 135 (1989) 177–195.

[15] S. Azimi, Free vibration of circular plates with elastic edge supports using the receptance method, *Journal of Sound and Vibration* 120 (1988) 19–35.

[16] S. Azimi, Free vibration of circular plates with elastic or rigid interior support, *Journal of Sound and Vibration* 120 (1988) 37–52.

[17] S. Azimi, J.F. Hamilton, W. Soedel, The receptance method applied to the free vibration of continuous rectangular plates, *Journal of Sound and Vibration* 93 (1984) 9–29.

[18] D.T. Huang, E.C. Ting, Vibration of plates with sub-structural deflections: a reverse receptance approach, *Journal of Sound and Vibration* 271 (2004) 177–207.

[19] I.D. Wilken, W. Soedel, The receptance method applied to ring-stiffened cylindrical shells: analysis of modal characteristics, *Journal of Sound and Vibration* 44 (1976) 563–576.
[20] I.D. Wilken, W. Soedel, Simplified prediction of the modal characteristics of ring-stiffened cylindrical shells, *Journal of Sound and Vibration* 44 (1976) 577–589.
[21] D.T. Huang, W. Soedel, On the free vibrations of multiple plates welded to a cylindrical shell with special attention to mode pairs, *Journal of Sound and Vibration* 166 (1993) 315–339.
[22] D.T. Huang, W. Soedel, Study of the forced vibration of shell-plate combinations using the receptance method, *Journal of Sound and Vibration* 166 (1993) 341–369.
[23] D.T. Huang, W. Soedel, Natural frequencies and modes of a circular plate welded to a circular cylindrical shell at arbitrary axial positions, *Journal of Sound and Vibration* 162 (1993) 403–427.
[24] A. Achong, Vibrational analysis of mass loaded plates and shallow shells by the receptance method with application to the steelpan, *Journal of Sound and Vibration* 191 (1996) 207–217.
[25] G.P. Zhang, Y.M. Huang, W.H. Shi, W.P. Fu, Predicting dynamic behaviors of a whole machine tool structure based on computer-aided engineering, *International Journal of Machine Tools & Manufacture* 43 (2003) 699–706.
[26] T.L. Schmitz, Predicting high-speed machining dynamics by substructure analysis, *Annals of the CIRP* 49 (1) (2000) 303–308.
[27] T.L. Schmitz, M.A. Davies, M. Kennedy, Tool point frequency response prediction for high-speed machining by RCSA, *ASME Journal of Manufacturing Science and Engineering* 123 (2001) 700–707.
[28] T.L. Schmitz, M.A. Davies, K. Medicus, J. Snyder, Improving high-speed machining material removal rates by rapid dynamic analysis, *Annals of the CIRP* 50 (1) (2001) 263–268.
[29] S.S. Park, Y. Altintas, M. Movahhedy, Receptance coupling for end mills, *International Journal of Machine Tools and Manufacture* 43 (2003) 889–896.
[30] A.S. Yigit, A.G. Ulsoy, Dynamic stiffness evaluation for reconfigurable machine tools including weakly non-linear joint characteristics, *Proceedings of the I MECH E Part B Journal of Engineering Manufacture* 216 (2002) 87–101.
[31] J.V. Ferreira, Transfer report on research: dynamic response analysis of structures with nonlinear components, internal report 96002, Dynamics Section, Department of Mechanical Engineering, Imperial College, London, 1996.
[32] J.V. Ferreira, D.J. Ewins, Nonlinear receptance coupling approach based on describing functions, *Proceedings of the 14th International Modal Analysis Conference* (IMAC-1996), Dearborn, MI, 1996, pp. 1034–1040.
[33] E.R. Marsh, A.H. Slocum, An integrated approach to structural damping, *Precision Engineering* 18 (1996) 103–109.
[34] J.C. Ziegert, R. Sterling, C. Stanislaus, T.L. Schmitz, Enhanced damping in long slender endmills, *Transactions of the 2004 North American Manufacturing Research Institute of SME* 32 (2004) 1–7.
[35] R. Blevins, *Formulas for Natural Frequency and Mode Shape*, Van Nostrand Reinhold Co., New York, NY, 1979.
[36] T.L. Schmitz, T. Burns, Receptance coupling for high-speed dynamics prediction, *Proceedings of the 21st International Modal Analysis Conference* (IMAC-2003), Kissimmee, FL, 2003 (on CD).
[37] W. Weaver, P. Timoshenko, D. Young, *Vibration Problems in Engineering*, fifth ed., Wiley, New York, 1990.
[38] T. Yokoyama, Vibrations of a hanging Timoshenko beam under gravity, *Journal of Sound and Vibration* 141 (1990) 245–258.
[39] J. Hutchinson, Shear coefficients for Timoshenko beam theory, *Journal of Applied Mechanics* 68 (2001) 87–92.